The origins of a wind turbine tip vortex

Daniel Micallef[1,2], Busra Akay[1], Carlos Simão Ferreira[1], Tonio Sant[2], Gerard van Bussel[1]

(1) DUWIND, Delft University of Technology, Kluyverweg 1, 2629HS Delft, The Netherlands.
(2) University of Malta, Faculty of Engineering, Department of Mechanical Engineering, Msida, MSD2080, Malta.

E-mail: daniel.micallef@um.edu.mt

Abstract. The tip vortex of a wind turbine rotor blade originates as a result of a complex distribution of vorticity along the blade tip thickness. While the tip vortex evolution was extensively studied previously in other work, the mechanism of the initiation of the tip vorticity in a 3D rotating environment is still somewhat obscured due to lack of detailed experimental evidence. This paper therefore aims at providing an understanding of how tip vorticity is formed at the wind turbine blade tip and what happens just behind the tip trailing edge. Stereo Particle Image Velocimetry (SPIV) is used to measure the flow field at the tip of a 2m diameter, two-bladed rotor at the TU Delft Open Jet Facility (OJF). The rotor has a rectangular blade tip. Spanwise measurements were performed for both axial and yawed flow conditions with a very small azimuthal increment. A 3D, unsteady, potential flow panel method is also used for the purpose of better understanding the tip bound vorticity. A validation study is carried out with positive results. This paper is focused on axial flow results.

A complex distribution of vorticity is found along the blade tip thickness. Just after release, the tip vortex becomes almost immediately round and well defined. Observations from the MEXICO rotor are confirmed again by a slight inboard convection of the tip vortex. This is explained by means of the effect of chordwise vorticity at the tip from the numerical solutions.

The results presented in this work suggest that a more physical interpretation of the tip loss effect is required. Currently, inclusion of tip effects are based primarily on either wake induced effects or on an empirical 3D correction for airfoil data. This research should stimulate a more rigorous approach, where the effects of the blade tip chordwise vorticity are implemented in tip correction models.

1. Introduction

1.1. Current state of the art

The wind turbine tip vortex characteristics have been extensively studied in previous works such as those by Grant et al.[2], Vermeer et al.[6, 7, 8] and lately for the MEXICO rotor by Lutz et al.[4]. These studies however focus on vortex structures considerably after their release and eventual roll-up. The mechanism of tip vortex generation on a wind turbine blade tip is still poorly understood and lacks detailed experimental evidence.

Current tip loss models are based on inductions which result due to the finite number of blades on a rotor. No consideration of what happens locally at the blade tip is made. This implies that a rethinking of the modelling of the tip needs to be performed. This becomes essential when trying to predict the drop in loading towards the blade tip region.

Much of the interest on the 3D corrections of aerofoils has been mostly devoted to the root regions of the blade. The phenomenon of stall delay, as its name implies, results due to the flow three-dimensionality caused by centrifugal effects on the boundary layer initiating Coriolis forces. This causes the stall phenomenon to occur at a higher angle of attack. The attached flow regime remains unchanged. The blade tip aerofoil characteristics have been given little consideration in literature. Data from the NREL UAE Phase VI rotor shows a strong reduction in the lift coefficient at the tip. The 3D derived aerofoil polar curves for the lift coefficient at the tip were found to be shifted to the right (to a higher angle of attack). Ang et al.[1] attribute this to three-dimensional effects due to the tip but do not specify what causes the reduction in lift at the same angle of attack as the 2D aerofoil data.

In this paper, the experimental observation of tip vortex formation and release is presented with particular attention to vorticity magnitude and kinematics. This provides a sound basis for 3D aerofoil models based on physical observations rather than empirical corrections.

1.2. Rotor

The TU Delft experimental rotor used in this study is a 2m diameter, two-bladed model rotor. A DU96-W180 aerofoil profile is used for the entire span of the blade except the root where the section transition to a cylindrical section for the connection with the hub. In this paper, some results are compared with the MEXICO rotor which is a 4.5m diameter, three-bladed rotor tested in the German-Dutch wind tunnel (DNW) having an open test cross section of 9.5 m x 9.5 m. The chord and twist distributions for both rotors are shown in Figure 1.2.

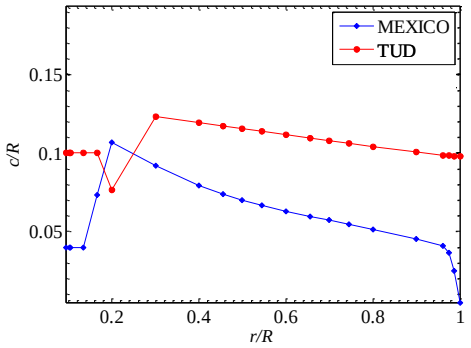

Figure 1. Comparison of the chord variation with rotor radius between the TUDelft and MEXICO rotors. Both axis are normalized with rotor radius.

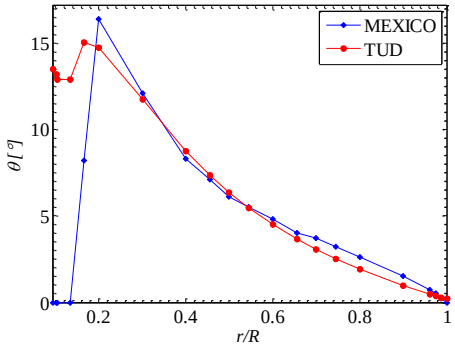

Figure 2. Comparison of the twist variation with rotor radius between the TUDelft and MEXICO rotors. The x-axis is normalized with the rotor radius.

2. Experiment description

The TU Delft SPIV experiment was carried out in the Open Jet Facility (OJF) wind tunnel at TU Delft. Both force (total thrust and torque) and SPIV measurements were carried out. The force measurements were performed using in-built rotor strain gauges fitted in the nacelle. The results of thrust and torque where used to generate thrust coefficient and power coefficient against tip speed ratio curves as shown in Figures 3 and 4. The uncertainty bars indicate standard deviations in the data.

Axial and yawed flow conditions (30° yaw) have been measured at an optimized tip speed ratio of 7. Also, off-design conditions at a tip speed ratio of 5 were measured for the axial flow

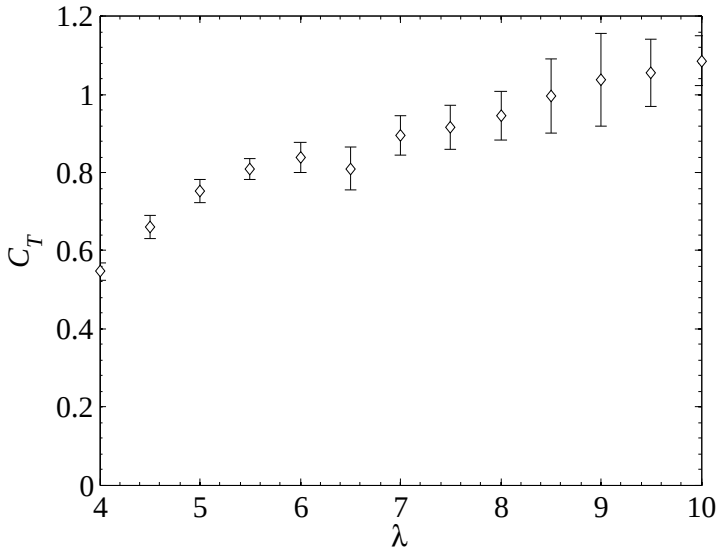

Figure 3. Thrust coefficient against tip speed ratio for axial flow conditions.

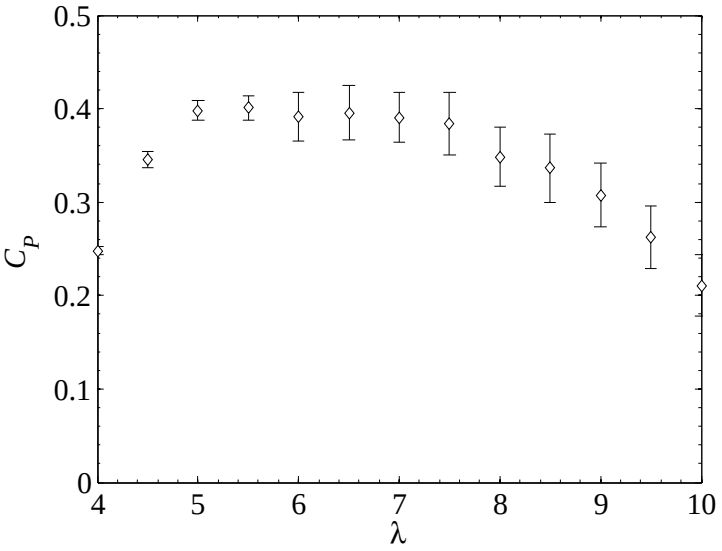

Figure 4. Power coefficient against tip speed ratio for axial flow conditions.

case. In this paper only the axial flow case at a tip speed ratio of 7 is presented.

The SPIV measurements were carried out in both chordwise and spanwise flow. For the spanwise measurements, the cameras were located below the blades with an angle of around 45° in order to obtain an accurate estimate of the out of plane velocity component (in this case the tangential velocity component). The laser was on the other hand located on a horizontal plane such that it is triggered when the blade reaches an azimuthal position of 90°. The setup is shown in Figure 5(a)

For the chordwise measurements, the cameras were placed on the side and the laser pulses shooting from below. Due to theshadowing effect, if the laser beam is directed from below the blade, the trailing edge region would be in shadow and no velocity vectors can be obtained from this region. To solve this, two sets of measurements had to be carried out. In the first set, the

laser beam is directed to illuminate the pressure side of the blade. In the second set, the beam is directed to illuminate the suction side. During the image processing, the two images are then combined to give a complete view of the flow around the blade. The setup for the chordwise measurements is depicted in Figure 5(b).

For yawed flow, the laser and cameras were rotated by the same yaw angle of the turbine such that fields of views relative to the blade are unchanged compared to the axial flow case. The setups used in the measurements are shown in Figure 5. Some photographs of the different setups are also shown in Figure 6.

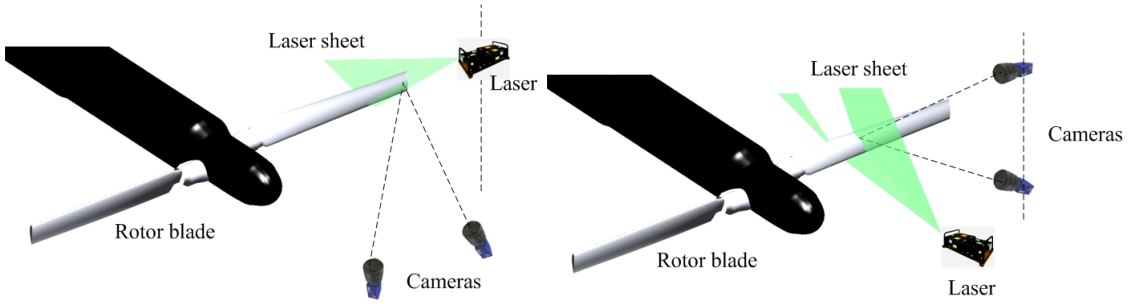

(a) Spanwise measurements (b) Chordwise measurements

Figure 5. Experimental setups for the TU Delft experiment.

Figure 6. Photograph of experimental setup for the TU Delft experiment.

Detailed image acquisition specifications are given in Table 1.The laser is used to illuminate the flow field. In this experiment, a double pulsed Nd:YAG laser use used with an energy per pulse of 200mJ. The laser sheet thickness was 3mm. The laser pulse separation was $80\mu s$

3. 3D, unsteady potential-flow vortex model

The 3D unsteady potential flow panel model is able to simulate the behaviour of time dependent motions of bodies such as wind turbine blades using a number of suitable boundary conditions. The formulation used for this model is based on that proposed by Katz & Plotkin [3]. The bodies are discretized into panel elements using sources and doublets. The doublets are released in the wake at the trailing edge for every time step by using the Kutta condition:

Table 1. Specifications of the image acquisition parameters for the TU Delft axial flow experiment.

	Axial flow
Camera	Imager Pro LX ×2
Focal Length	180mm
Resolution	4066pi × 2708pi
Diaphragm aperture	5.6 (both cameras)
Field of view	262.8mm × 176.23mm
Recordings	100 image pairs
Laser pulse separation	$\Delta t = 80\mu s$
Freestream pixel shift	8pi
Scale factor	13.85pi/mm
Spatial resolution	2.31mm (using 32×32 window size)

$$\mu_{Wt} = (\mu_u - \mu_l)_t \tag{1}$$

Where μ is the doublet strength, W refers to the wake, u the upper surface of the blade, ℓ is the lower surface and t is the time.

The kinematic motion of the bodies is determined and can be represented in general by a translation and a rotation which can be described by the following equation:

$$\frac{\partial \Phi}{\partial n} = (\vec{U_\infty} + \vec{V_{rel}} + \vec{\Omega} \times \vec{r}).\vec{n} \tag{2}$$

where Φ is the velocity potential, n is the normal direction to a particular surface, U_∞ is the wind speed, V_{rel} is the relative velocity Ω is the rotational speed, r is the position coordinate along the body. The algorithm for the panel model methodology is given here.

(i) Input the following primary information
- Number of bodies (including nacelle and blades)
- Body discretization: choose number of spanwise and chordwise panels (a cosine distribution of elements is used)
- Number of rotor revolutions
- Azimuthal angle increment per time step
- Freestream speed and direction and rotor speed in RPM
- Additional parameters such as vortex initial core size and vortex core and core growth model

(ii) Initialize the simulation using an initial estimate of the source and doublet distribution on the bodies.

(iii) Rotate the turbine blades by using the general motion function shown in eqn. 2.

(iv) Determine the wake strength using the Kutta condition at the trailing edge (eqn.1).

(v) Calculate the source and doublet distribution using eqn.3 for the time-step being considered.

$$\sum_{k=1}^{N} C_k \mu_k + \sum_{i=1}^{N_w} C_i \mu_i + \sum_{k=1}^{N} B_k \sigma_k = 0 \tag{3}$$

where C is a constant coefficient and σ is the source strength.

(vi) Using the Biot-Savart law, calculate the velocity at every wake vertex point. A first order scheme is used to update the position of each wake vertex after a time interval determined by the azimuthal increment determined by the user.

(vii) Repeat until all time-steps have been evaluated.

(viii) Estimate the pressures acting on each body element.

(ix) Calculate any required output such as the body loading and velocity field.

3.1. Simulations

The simulations were carried out using the supercomputing cluster at the University of Malta having the following general specifications:

- 64 processing nodes, with 12 cores on each node
- 2TB of main memory, 32 GB per node
- 20 TB of disk space
- Infiniband DDR Interconnect

Table 2. Major input parameters in the numerical model. In this table, Ω = rotor rotational speed in RPM, λ = tip speed ratio, γ = rotor yaw angle.

Conditions	Chordwise panels	Spanwise panels	Revolutions	Azimuthal step	Vortex core size [m]
$\Omega = 400RPM$, $\lambda = 7$, $\gamma = 0°$, pitch $= 0°$	54	58	10	5	0.00882

4. Validation

The radial velocity is used to validate the numerical model with the experimental results. The radial flow component is particularly important for the understanding of the convection of the tip vortex. For the axial flow case with $\lambda = 7$ shown in Figure 7, the radial velocity is rather uniform before the blade passage at 80°. The comparison between the experimental and numerical results at this azimuth angle compare very well. When the blade is at 90° azimuth, some differences between the experimental and numerical results are apparent particularly at the blade's suction side. The computations show a smaller inboard radial velocity just downstream of the blade tip compared to the experimental result. Also, the region of inboard radial velocity seems to extend more inboard. This problem can be attributed to the panel model to capture precisely the variation in bound vorticity at the tip. After the tip vortex is released at 100°, the comparisons between simulations and experiment are good. Small differences in vortex core location may arise due to the numerical modelling of the vortex core. The effect is that the numerical model shows a larger distortion of the radial velocity flow field compared to the experimental observations.

These comparisons give further confidence on the validity of the results which will be presented in the next sections.

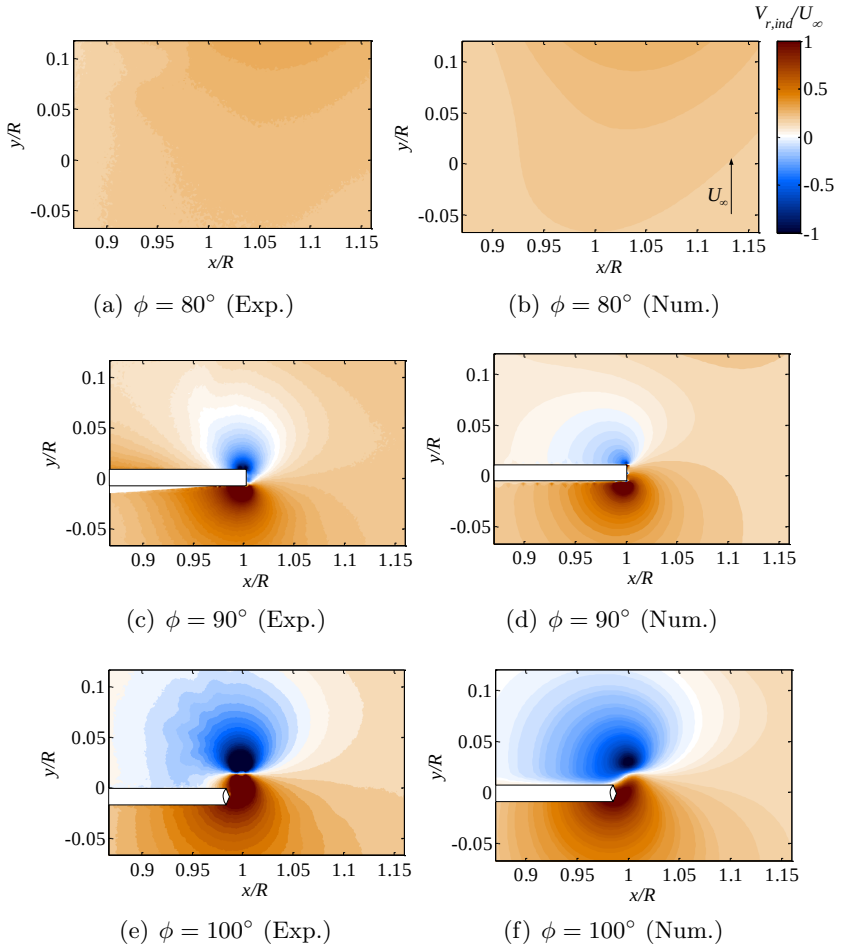

(a) $\phi = 80°$ (Exp.) (b) $\phi = 80°$ (Num.)

(c) $\phi = 90°$ (Exp.) (d) $\phi = 90°$ (Num.)

(e) $\phi = 100°$ (Exp.) (f) $\phi = 100°$ (Num.)

Figure 7. Validation of the calculated radial velocities using the SPIV phase-locked averaged results for the TU Delft rotor. Different blade azimuth angles are shown in the figures for axial flow at $\lambda = 7$. The y-axis is the direction normal to the rotor while the x-axis is in a horizontal plane. Both coordinates are normalized by rotor radius. The induced radial velocities are normalized with the free-stream velocity.

5. Results and discussion

5.1. Vorticity generation along blade thickness

As can be seen from Figures 8, a high vorticity region is formed starting from the leading edge. The convection of this vorticity can be seen to depend highly on the operating tip speed ratio (and hence wind speed). The variation of vorticity along the blade thickness can be observed along the blade chord. These features are direct signatures of the effects of chordwise bound vorticity. It must be noted that due to the obstruction of the blade on the view as well as the reflections from the blade tip, the pictured vorticity might not show the complete local vorticity distribution. This problem is of course only relevant when the blade is in the field of view. Behind the trailing edge, the vorticity convects and forms a symmetrical tip vortex.

In order to visualise better the tip vortex location, Figure 9 shows vorticity in the tip region for various blade azimuth positions. For azimuth angles from 90° to 94° the vorticity is seen to be distributed along the thickness. After this, the tip vortex is formed and the trailing vorticity sheet roll-up becomes apparent. The location of the maximum vorticity vortex core can be seen to be slightly inboard just after release. At $\phi = 130°$ the maximum vorticity can be found at

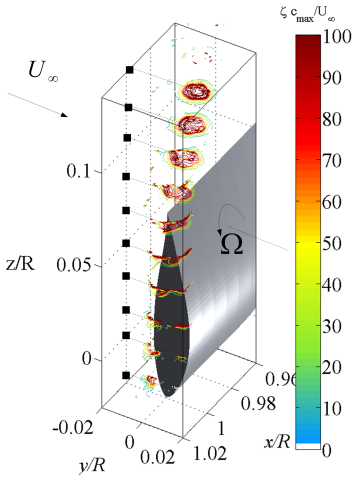

Figure 8. Origin and release of the blade tip vortex for axial flow at a tip speed ratio of $\lambda = 7$ with a pitch angle of 0°. The coordinate axis are normalized with rotor radius while the contours of vorticity are normalized with c_{max}/U_∞. The free-stream is from left to right.

around r/R = 1. This phenomenon has been pointed out and investigated by Micallef et al. [5] for the MEXICO rotor. In this paper, the study is extended to the TUDelft rotor.

5.2. Chordwise directed vorticity at the tip

Close to the rotor blade the effects of bound vorticity dominate the flow. The panel method enables the description of the vorticity distribution along the blade surface. The bound vorticity is spanwise over most of the blade span. In the tip region, the bound vorticity changes direction to chordwise. This is a well known phenomenon for finite wings. However, for the 3D rotating environment of a wind turbine blade the issue has not been thoroughly investigated in the past. In the context of this work, the interaction between released wake vorticity and the bound vorticity is of particular importance. Figure 10(a) shows the notation used for the subsequent Figures 10(b) and 10(c) which shows the normalized distribution of chordwise vorticity ($\frac{\partial \Gamma}{\partial r}$ in the tip region for the suction side and the pressure side.

As can be observed, the vorticity changes direction from spanwise to chordwise from around the 90% span position. The magnitude of the chordwise bound vorticity becomes particularly strong at the trailing edge region. This means that the effect of the bound vorticity on the wake becomes even more important. This effect on the released wake vorticity results in an important impact on the blade loading at the tip since inevitably, the wake kinematics become intrinsically linked to the magnitude of the chordwise bound vorticity.

5.3. Kinematics of the released tip vortex

The tendency of the tip vortex to exhibit a slight inboard convection just upon release has important practical implications since its position will influence the total wake inductions experienced at the tip. The numerical model is used to demonstrate that the body panels cause an inboard radial flow just behind the trailing edge which counteracts the expansion caused by the wake. This velocity component results due to the chordwise vorticity distribution discussed in the previous section. The radial flow field caused by the body panels (and hence bound vorticity) is shown in Figure 11. Although the calculated radial velocities are relatively small, the region of influence is quite large and extends to a large fraction of the tip region giving

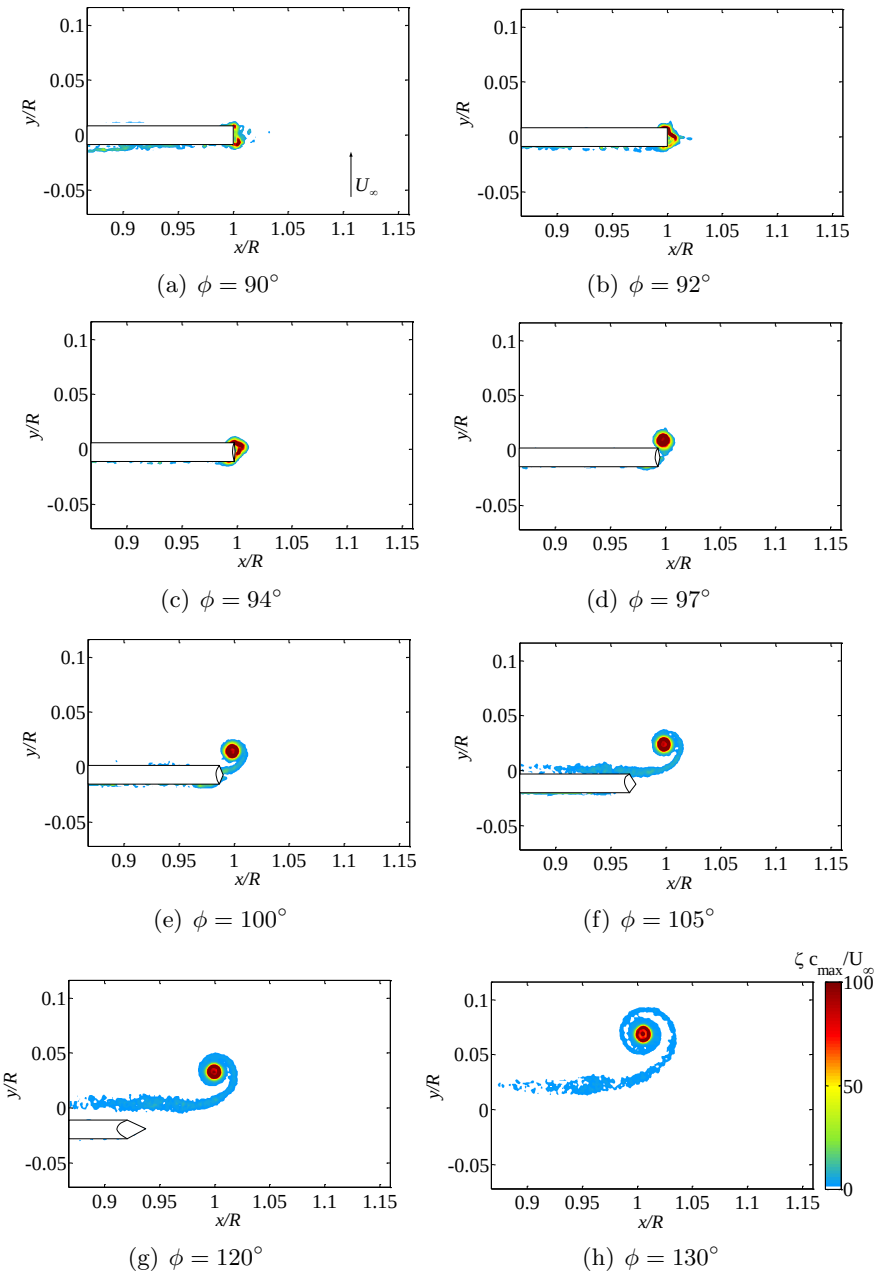

(a) $\phi = 90°$ (b) $\phi = 92°$

(c) $\phi = 94°$ (d) $\phi = 97°$

(e) $\phi = 100°$ (f) $\phi = 105°$

(g) $\phi = 120°$ (h) $\phi = 130°$

Figure 9. Tip vorticity origin and release for axial flow at $\lambda = 7$ with a pitch of 0°. Results are shown on a horizontal plane at the 90° azimuth position and for various azimuthal blade positions ϕ. The vorticity contours are normalized with c_{max}/U_∞.

a possible reason for the observed motion of the tip vortex upon release. A similar observation has also been made by Micallef et al. [5] for the MEXICO rotor.

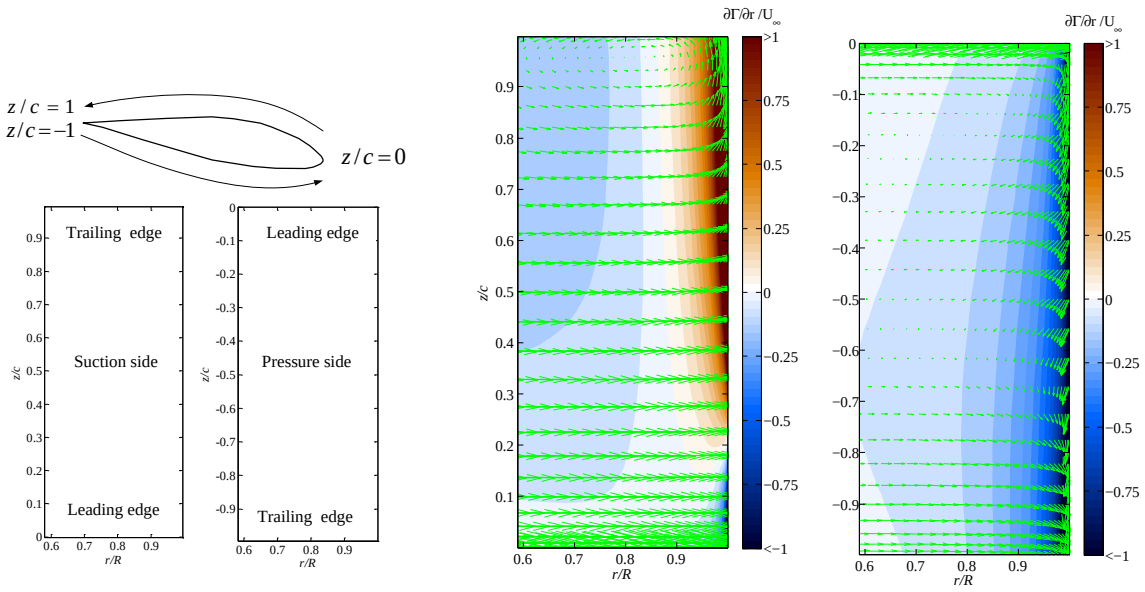

(a) Coordinate notation (b) $\phi = 90°$ (c) $\phi = 92°$

Figure 10. Contour plots showing blade surface chordwise vorticity on the suction side (SS) $(0 < z/c < 1)$ and the pressure side (PS)$(-1 < z/c < 0)$ for the TU Delft rotor in axial flow at a tip speed ratio $\lambda = 7$ and pitch angle of 0°. In each of the plots 10(b) and 10(c) the chordwise directed vorticity is normalized with the free-stream velocity.

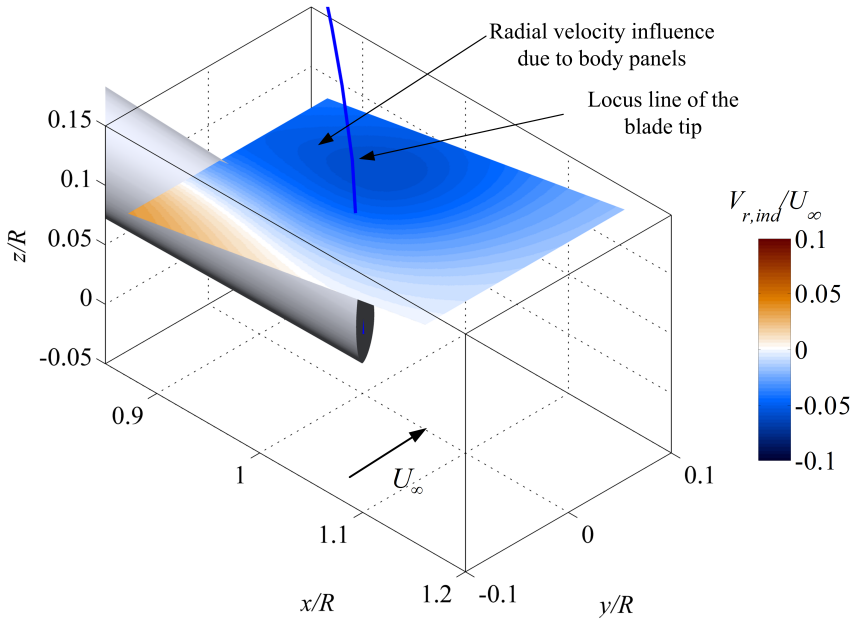

Figure 11. Influence on the radial velocity component (on a plane) due to the body panels. The locus line of the blade tip quarter-chord motion is also shown. The coordinate axis are normalized with rotor radius and the radial flow velocity is normalized with the free-stream velocity

5.4. A comparison of observations

Figure 12 compares the location of the tip vortices 10° after the blade passage. Figure 12(c) also shows the comparison of bound vorticity for both the MEXICO and TU Delft rotor as obtained from the panel model. For the MEXICO rotor, the vortex core is smaller due to the differences in the variation of geometry and lift (resulting in differences in bound vorticity). The differences in the downstream location of the tip vortex is due to the virtually unloaded tip of the MEXICO rotor and the highly loaded tip of the TU Delft. The differences in the operating tip speed ratios is very small so this effect is not expected to cause differences in the normalized tip vortex locations.

The inboard location of the tip vortex for the MEXICO rotor is clear. For the TU Delft rotor, the tip vortex center is also located slightly inboard. The impact of this phenomenon is particularly relevant for the determination of the axial inductions at the tip which will ultimately effect the angle of attack, and hence the tip loading. This experimental evidence points towards the need of revised wake expansion models to take into account this behaviour.

6. Conclusions

This experimental and numerical study gives detailed physical insight of the development and release of the tip vortex. The SPIV results have shown a rather complex distribution of vorticity along the blade thickness. Once released at the trailing edge, the tip vorticity rapidly becomes round and symmetrical. The tip vortex does not immediately move outboard thus confirming previous studies by Micallef et al. [5] for the MEXICO rotor. This has been attributed to strong chordwise bound vorticity present over the 10% span from the tip. For both the TU Delft and the MEXICO rotor, the tip vortex is found inboard of the tip even after 10° azimuth after release.

This work gives a new direction for improving tip loss modelling based on physical observations. In future work, the effect of off-design tip speed ratio and yaw angle will be considered.

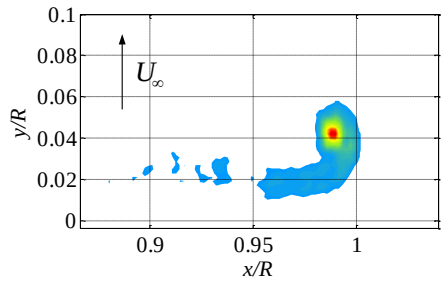

(a) Vorticity normalized with c_{max}/U_∞ for the MEXICO rotor

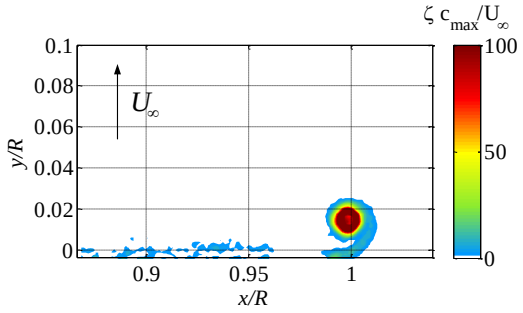

(b) Vorticity normalized with c_{max}/U_∞ for the TU Delft rotor

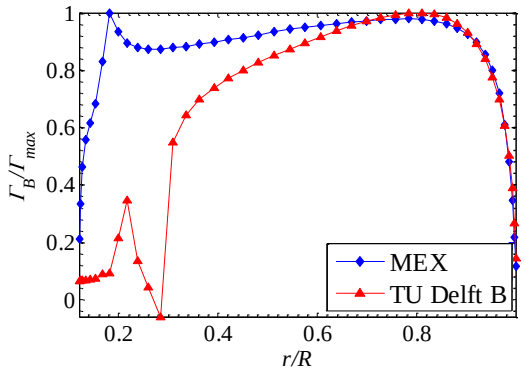

(c) Bound vorticity against normalized rotor radius comparison between the MEXICO and the TU Delft rotor as obtained from the panel model. The bound vorticity is normalized with the maximum bound vorticity on the blade.

Figure 12. MEXICO rotor ($\lambda = 6.67$) and TU Delft rotor ($\lambda = 7$) tip vortex motion 10° after the blade passage. The bound vorticity variation is also shown for the same operating conditions in order to compare differences.

References

[1] H. Ang, W. Shen, J.N Sørensen, and W. Zhu. Investigation of load prediction on the mexico rotor using the technique of determination of the angle of attack. *CHINESE JOURNAL OF MECHANICAL ENGINEERING*, 23(1), 2011.

[2] I. Grant, M. Mo, X. Pan, P. Parkin, J.Powell, H. Reinecke, K. Shuang, F. Coton, and D. Lee. An experimental and numerical study of the vortex filaments in the wake of an operational, horizontal-axis, wind turbine. *Journal of Wind Engineering and Industrial Aerodynamics*, 23, no.6:513–519, 2000.

[3] J. Katz and A. Plotkin. *Low-Speed Aerodynamics*. Cambridge University Press, second edition, 2001.

[4] T. Lutz, K. Meister, and E. Krämer. Near wake studies of the mexico rotor. In *In proceedings of the EWEC conference*, pages 161–165, March 2011.

[5] Daniel Micallef, Gerard van Bussel, Carlos Simao Ferreira, and Tonio Sant. An investigation of radial velocities for a horizontal axis wind turbine in axial and yawed flows. *Wind Energy*, pages n/a–n/a, 2012.

[6] LJ Vermeer, JJ Briaire, and C. van Doorne C. How strong is a tip vortex? In *In: British Wind Energy Association Annual Wind Energy Conference, Warwick, UK*, page 5964, 1995.

[7] N Vermeer. How fast is a tip vortex? In *In: Nineth IEA Symposium on the Aerodynamics of Wind Turbines, Stockholm, Sweden*, pages 15–20, 1995.

[8] N Vermeer. How big is a tip vortex? In *In: Tenth IEA Symposium on the Aerodynamics of Wind Turbines, Edinburgh, UK*, pages 77–82, 1996.